Computational Energy Science

Vol. 1, No. 2, p. 69-85, 2024

Original article

Study on the pattern of hydraulic fracture propagation and fracture conductivity of conglomerate with different lithologies in Ma'nan area

Shuiqing Hu[1], Chunlei Wei[2], Yiqun Yan[1], Daobing Wang[2]*, Yiping Ye[3], Xiaoshan Li[3], Jing Zhang[3], Zhongchen Ba[3]

[1]*Research Institute of Petroleum Exploration and Development, PetroChina, Beijing 100083, P. R. China*

[2]*School of Mechanical Engineering, Beijing Institute of Petrochemical Technology, Beijing 102617, P. R. China*

[3]*Xinjiang Oilfield Company, PetroChina, Karamay 834000, P. R. China*

Keywords:
Conglomerate
true triaxial
hydraulic fracturing
fracture conductivity
fracture propagation

Cited as:
Hu, S., Wei, C., Yan, Y., Wang, D., Ye, Y., Li, X., Zhang, J., Ba, Z. Study on the pattern of hydraulic fracture propagation and fracture conductivity of conglomerate with different lithology in Ma'nan area. Computational Energy Science, 2024, 1(2): 69-85.
https://doi.org/10.46690/compes.2024.02.02

Abstract:
The Ma'nan Fengcheng Formation in Xinjiang is rich in oil and gas resources, offering significant exploration potential. The reservoir's lithology is diverse, comprising dolomitic, tuffaceous, and sandy conglomerates. However, the patterns of hydraulic fracture propagation and variations in fracture conductivity in these formations are not well understood. To address this, we conducted experiments using a true triaxial hydraulic fracturing physical modeling system and a fracture conductivity testing system. Our key findings are as follows: In sandy conglomerate reservoirs, fractures tend to propagate along the direction of maximum horizontal stress. The presence of gravel causes these fractures to develop into a complex network of narrower microfractures. The breakdown pressure hierarchy is Dolomitic > Tuffaceous > Sandy conglomerate. Increased confining pressure raises the fracture pressure across all lithologies. Fracture conductivity decreases with increasing confining pressure, particularly during the initial stages of pressure loading, and this loss is irreversible. The conductivity hierarchy is Sandy > Dolomitic > Tuffaceous conglomerate. Additionally, increasing the proppant concentration from 2 to 6 kg/m^2 enhances fracture conductivity by approximately 1.5 times. These findings provide valuable insights and technical support for the efficient development of conglomerate reservoirs in China.

1. Introduction

Western China, including the Junggar Basin, Tarim Basin, Bohai Bay Basin, and Songliao Basin, boasts numerous conglomerate oil reservoirs. In the Mahu Depression alone, located in the Junggar Basin's center, up to 17.6 × 10^8 t of Conglomerate oil reservoirs have been discovered (Zhi et al., 2021). Despite this wealth, China's foreign dependence on crude oil and natural gas exceeds 70% and 50%, respectively (Wang et al., 2015). Efficient development of conglomerate reservoirs is crucial to meeting the nation's energy needs, ensuring energy security, and maintaining stability (Li et al., 2023).

The Permian Fengcheng Formation conglomerate reservoir in the central area of the Mahu Depression, Junggar Basin, is characterized by deep burial, complex lithology, high density, and tightness, resulting in often low extraction efficiency. Hydraulic fracturing technology is essential for developing tight conglomerate oil and gas reservoirs (Li et al., 2020; Liu, 2021). This technique involves pumping high-pressure water and additives into the wellbore to create fractures with high conductivity when the injection pressure exceeds the reservoir's tensile strength (Chen, 2022). However, fractures formed during hydraulic fracturing may close under confining pressure, reducing their conductivity and diminishing production enhancement (Cooke Jr, 1973). To address this issue, the

Yandy Scientific Press

*Corresponding author.
E-mail address: hushuiqing@petrochina.com.cn (S. Hu); 2745893398@qq.com (C. Wei); yanyiqun@petrochina.com.cn (Y. Yan); upcwdb@hotmail.com (D. Wang); upcwdb@bipt.edu.cn (D. Wang); yeyp@petrochina.com.cn (Y. Ye).

Received April 6, 2024; revised May 15, 2024; accepted June 6, 2024; available online June 9, 2024.

common approach is to inject proppant into the fractures. This ensures that the fractures maintain high conductivity even after fluid injection has stopped (McDaniel, 1986).

The presence of gravel in conglomerate reservoirs complicates fracture propagation, posing significant challenges to on-site fracturing construction. Understanding the factors affecting fracture propagation in these reservoirs is crucial (Wang et al., 2024a). Current methods for studying the fracture propagation mechanisms in conglomerate reservoirs can be broadly categorized into numerical simulations and true triaxial physical model experiments of hydraulic fracturing. Factors such as fracturing fluid viscosity, injection rate, gravel content, and ground stress differences impact fracture propagation (Wang et al., 2024). Geertsma and De Klerk (1969) conducted research indicating that the viscosity and injection rate of fracturing fluid have an impact on fracture propagation, although the specific influence remains unclear. Lian et al. (2009) utilized ABAQUS commercial software to establish a two-dimensional hydraulic fracturing numerical model of conglomerate reservoirs, investigating the effects of geological conditions and rock physical properties on fracture propagation. Their findings suggest that increased viscosity of the fracturing fluid can enhance fracture width (Liu et al., 2018). Li et al. (2013) using RFPA2D-Flow software, created a two-dimensional plane strain model. Their study revealed that larger gravel diameters hinder crack propagation but promote the formation of intricate fracture networks. Other research has highlighted that altering horizontal principal stress differences can reduce the pressure required for crack extension (Jiang et al., 2022). However, the influence of horizontal in-situ stress differences on fracture propagation is relatively minor, mainly influenced by the angle of approximation and the cohesion of bedding planes (Gong et al., 2019; Wang et al., 2024b). While numerical simulations are valuable, they rely on assumptions and simplified conditions, potentially introducing errors (Zhou et al., 2024). Therefore, conducting indoor true triaxial physical model experiments of hydraulic fracturing is essential for gaining a deeper understanding of the mechanisms and influencing factors involved in the formation of hydraulic fracture.

Laboratory experimental studies have revealed that the propagation of hydraulic fractures in conglomerate reservoris is influenced by multiple factors, including natural fracture characteristics and reservoir conditions. Among these factors, reservoir structure plays a crucial role in shaping fracture patterns during hydraulic fracturing operations, while the magnitude of differential stress is a decisive factor in determining whether fractures propagate horizontally or vertically (Yu et al., 2024). Meng et al. (2010) conducted hydraulic fracturing experiments on conglomerate rock samples, confirming that increasing the horizontal stress differential reduces the fracturing pressure of the rock (Yu et al., 2024). For horizontal in-situ stress differences less than 6 MPa, multiple fractures characterize the propagation pattern, facilitating the formation of fracture networks. Conversely, when the horizontal in-situ stress difference exceeds 9 MPa, single fractures tend to form. Shi et al. (2023) showed that despite high-viscosity fracturing fluid increasing fluid flow resistance, it accelerates liquid pressurization, leading to quicker artificial fracture formation in conglomerate samples. Cai et al. (2022) and Sun (2022) performed experiments on various conglomerate samples and observed that a higher gravel content results in more complex fracture geometries and increased branching cracks.

In the process of fracture propagation, hydraulic fracturing fractures are often closed under the action of confining pressure. Fracture closure will reduce the fracture conductivity and affect the effect of hydraulic fracturing. At present, people have studied the loss of conductivity in conglomerate reservoirs through numerical simulation, and have obtained some basic understandings. Numerical simulation studies have identified that the elastic modulus of the reservoir, closure pressure, and proppant particle size are primary factors influencing the conductivity of propped fractures. Wang et al. (2021) carried out conductivity loss experiments on sedimentary rocks such as conglomerate, and constructed a mathematical model of conductivity. The study found that the change of conductivity can be divided into two stages: the initial stage of closure and the stable stage of closure. In the initial stage of closure, fracture conductivity is mainly affected by factors such as proppant performance, concentration, reservoir lithology and closure pressure. During the closure and stabilization period, the conductivity of fractures is mainly influenced by the initial conductivity and the time required for proppant rupture, embedment, and rearrangement to establish a stable structure (Wang et al., 2023). Stegent et al. (2010) conducted a finite element analysis of the pressure around the perforation, and believed that the large particle size proppant is more conducive to improving the fracture conductivity. Fan et al. (2019) investigated the variation of fracture conductivity with increasing proppant concentration using the discrete element method. The simulation results show that when the proppant concentration increases, the change of fracture conductivity is divided into four stages. In the first and second stages, due to the small amount of proppant in the fracture, increasing the sand concentration is beneficial to the improvement of conductivity. During stages three and four, the heightened concentration of proppants within fractures causes permeability to decline more rapidly than the rate at which conductivity improves with increasing proppant concentration. Consequently, additional increments in proppant concentration do not support the retention of conductivity.

Numerical simulation usually needs to make a number of simplifications and assumptions when analyzing the loss of conductivity, and it is difficult to truly reflect the loss of conductivity of the fracture. Therefore, the laboratory experiment can truly reflect the pressure change inside the fracture and observe the loss of conductivity (Wang et al., 2024a). For example, Wang et al. (2023)'s experimental study found that under the same sand concentration conditions, larger particle proppants are more effective in enhancing conductivity. In addition, no matter what size of proppant is used, the fracture conductivity will decrease with the increase of closure pressure, but the conglomerate with larger particle diameter is beneficial to maintain higher conductivity. The decrease of fracture conductivity is largely due to the fact that the proppant is broken or embedded in the reservoir, which leads

to the narrowing of the fracture width. Therefore, the breaking, embedding and particle migration of the proppant will damage the fracture conductivity. In addition, the fracture conductivity is also related to the elastic modulus of the reservoir (Wang et al., 2020; Li et al., 2022; Liu et al., 2023). Zou et al. (2021) found that the proppant is obviously embedded in the rock plate in the sandy conglomerate with smaller gravel diameter, while the proppant is more likely to break in the sandy conglomerate with medium gravel diameter. Their also shows that the use of high proportion and high concentration of small particle size proppants helps proppants migrate in fractures, thereby improving the conductivity of proppants. Xie et al. (2011) studied the loss of fracture conductivity of conglomerate with different gravel contents, and found that the conductivity was the best when the gravel content was 40% - 60%.

Currently, extensive research has focused on hydraulic fracturing's fracture propagation mechanisms and fracture conductivity (He, 2022). However, systematic studies on conglomerates, particularly in the complex Lower Permian Fengcheng Formation of the central Mahu Sag, are relatively scarce (Yang et al., 2021). Reservoirs in this region consist mainly of tuffaceous conglomerate and dolomitic conglomerate, with complex lithologies that pose challenges for differentiation. Predicting post-fracturing fracture morphology and understanding conductivity loss after proppant placement remain unclear.

Hence, this study conducts and conductivity loss experiments on various lithologies of tight conglomerate reservoirs in the Ma'nan area. It aims to analyze the fracture propagation morphology and corresponding conductivity loss of different lithologies during the fracturing process. By investigating the variations in fracture propagation morphology and conductivity loss among different lithologies, it offers a solid foundation for devising distinct construction schemes for reservoir development in the Ma'nan area.

2. Experimental preparation and process

2.1 Rock sample preparation

The oil and gas reservoirs in the Ma'nan area predominantly comprise tight conglomerate formations, characterized by deep burial and complex lithology. These formations consist mainly of tuffaceous conglomerate and dolomitic conglomerate. However, conglomerate is typically loose, with weak binding forces between rock particles, posing challenges in obtaining drilling rock samples from conglomerate reservoirs in the Ma'nan area (Chen, 2022). To address this issue, natural conglomerate outcrops resembling the actual reservoir lithology were selected for conducting relevant rock mechanics experiments in this study.

As shown in Fig. 1, the rock sample used in the true triaxial hydraulic fracturing physical model experiment is a cube with dimensions of 100 mm × 100 mm × 100 mm. To ensure uniform stress distribution, all six surfaces of the rock sample are meticulously polished to mitigate stress concentration resulting from unevenness. Next, a circular hole with a diameter of 16 mm and a depth of 60 mm is drilled at the center of the top surface of the cube. Finally, a steel pipe is securely affixed to the inner wall of the drilled hole using epoxy resin, leaving a 10 mm open section at the bottom of the steel pipe and the bottom of the hole.

Fig. 1. Rock sample for the physical model experiment of true triaxial hydraulic fracturing.

The rock plate utilized in the fracture conductivity experiment, as illustrated in Fig. 2, adheres to API standards, boasting a length of 177.2 mm, a width of 38 mm, and a thickness of 20 mm. To ensure compatibility with the diversion chamber, the two ends of the rock plate are machined into a circular shape, maintaining parallelism within a tolerance of ± 0.08 mm.

Fig. 2. Rock samples for conductivity experiments: (a) Top surface; (b) Side surface.

To ensure the efficacy of the conductivity test experiment, proper sealing of the rock plate is imperative. Initially, transparent tape is affixed to the upper and lower surfaces of the rock plate to safeguard it against sealant adhesion, thereby preserving the surface parallelism. Subsequently, surplus tape is removed, and vulcanized silicone adhesive is uniformly applied around the rock plate. Following this, a 24-hour waiting period ensues to allow for complete curing of the adhesive. Upon full curing, the transparent tape on the upper and lower surfaces of the rock plate is removed.

2.2 Experimental equipment

The physical simulation system for true triaxial hydraulic fracturing comprises a true triaxial experimental loading frame, triaxial hydraulic stabilizer, an ISCO pump, and a data acquisition and processing system, as depicted in Fig. 3. During the experiment, the three principal planes of the rock sample undergo loading from triaxial hydraulic stabilizer to emulate the maximum horizontal stress, minimum horizontal stress, and vertical in-situ stress. This setup enables the simulation of hydraulic fracture initiation, diversion, and extension within the sample under specific three-dimensional

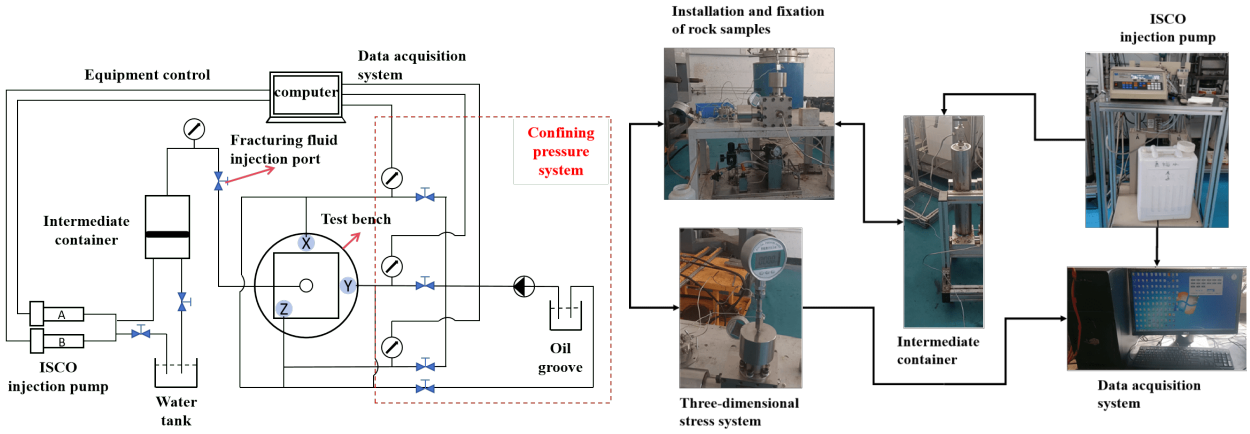

Fig. 3. True triaxial hydraulic fracturing physical model experimental equipment flow diagram and experimental flow diagram: (a) Equipment process diagram and (b) Experimental flow chart.

stress conditions. The detailed steps of the hydraulic fracturing physical model experiment are outlined as follows:

1) Clean the intermediate container and pipeline thoroughly to ensure no drug residue remains in the true triaxial hydraulic fracturing simulation system.
2) Connect and inspect the internal pipeline of the system to verify there are no leaks.
3) Inject the prepared fracturing fluid (0.4% guar gum + 0.15% crosslinking agent + 0.04% citric acid) into the intermediate container for backup.
4) Place the prepared rock sample onto the test bench and tighten the bolts sequentially to securely and reliably install the rock sample inside the instrument.
5) Use the pipeline to link the steel wellbore with the intermediate vessel and the ISCO pump.
6) Apply on the three main planes of the rock sample using a vacuum pumping pump to simulate the actual stress difference.
7) Initiate the ISCO injection pump, while the data acquisition system records the injection pressure in the wellbore every second.
8) Disassemble the equipment and rock samples, then observe and document the fracture morphology.

The fracture conductivity monitoring system comprises a servo pressurization system, flow monitoring system, and data acquisition system. Throughout the experiment, confining pressure is exerted on the upper and lower pistons of the fracture condutivity chamber to replicate the ground stress-induced closure effect on the fracture surface in actual formation conditions. The equipment's maximum confining pressure capability extends to 120 MPa, adequately fulfilling the evaluation criteria for fracture conductivity under real formation conditions.

Fig. 4 shows the experimental equipment diagram (a), the fracture condutivity chamber separation diagram (b), and the experimental flow chart (c). In the split diagram of the fracture condutivity chamber, A represents the proppant with different concentrations used in the experiment. B indicates the fracture surface supported by the proppant. In practical engineering, this is the fracture surface; in this experiment, it is represented by guide plates of different lithologies. E and D are the upper and lower pistons. The hydraulic press simulates the high confining pressure state in the actual formation by applying pressure to the upper and lower pistons. J is the sealing ring to prevent the liquid from flowing out of the instrument. G is the differential pressure sensor hole, and the conductivity is calculated by recording the differential pressure changes at different positions in the instrument. The step-by-step experimental procedure is outlined as follows:

1) Cleanse the fracture condutivity chamber, upper and lower pistons, and the filter screen meticulously to prevent any residual proppant from affecting the experimental apparatus or data accuracy.
2) Sequentially assemble the rock sample, proppant, fracture conductivity and lower pistons, and other components inside the flow chamber as illustrated in the schematic diagram of proppant fracture condutivity chamber according to API standard.
3) Position the assembled fracture conductivity chamber onto the pressure platform, ensuring the upper platform of the hydraulic press makes close contact with the piston on the fracture conductivity chamber by rotating the clockwise disc. Connect the fracture conductivity chamber to the ISCO pump and the differential pressure meter via the pipeline.
4) Utilize the computer-controlled hydraulic pressure platform to apply 0.5 MPa pressure to the fracture condutivity chamber, ensuring optimal contact between the fracture condutivity chamber components.
5) Flush the fracture condutivity chamber and pipeline with deionized water, expelling any air from the experimental equipment. Continue rinsing for at least 1-minute post-bubble discharge, until the pressure difference sensor returns to zero under no flow conditions.

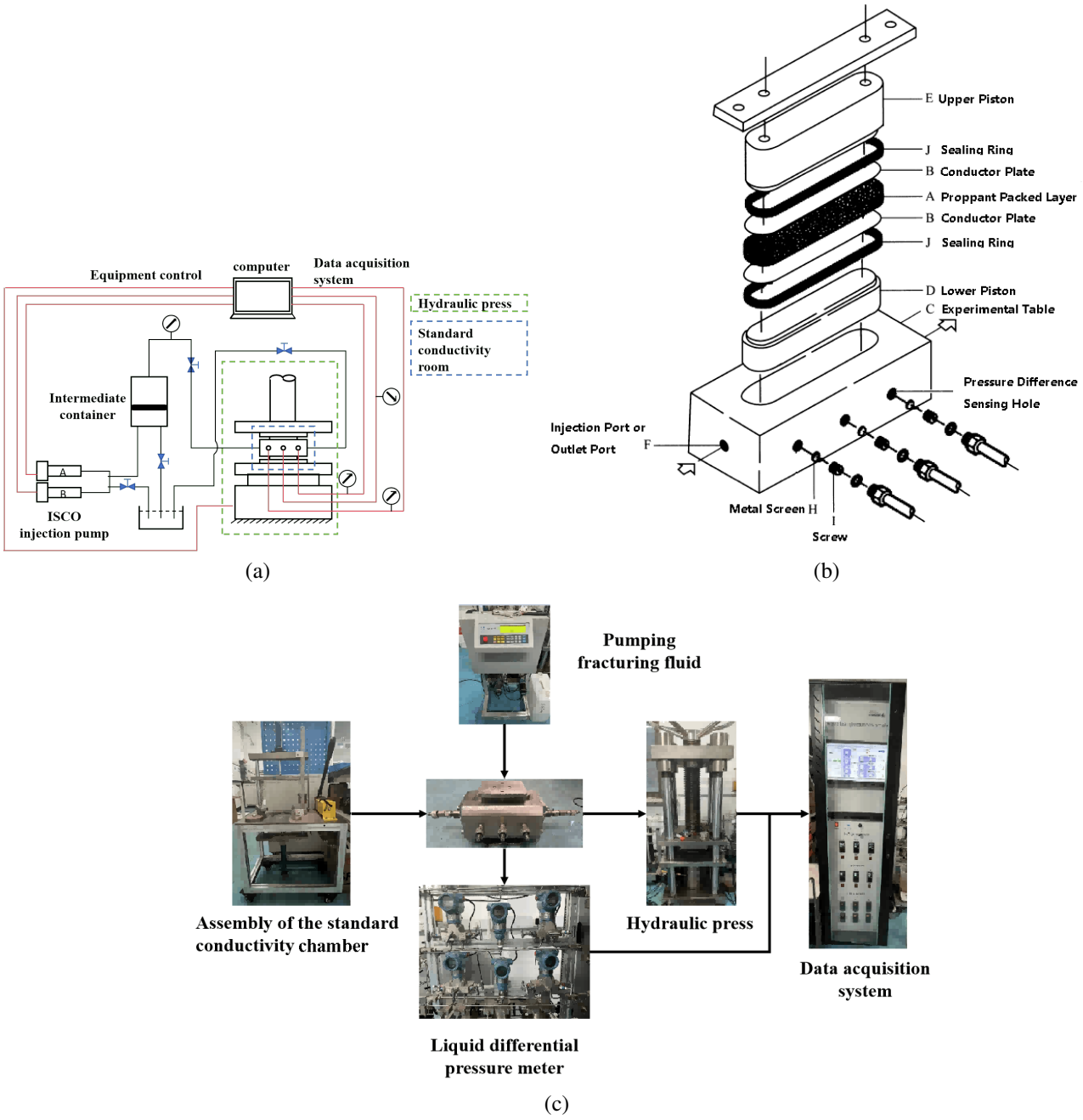

Fig. 4. Fracture conductivity monitoring equipment and process diagram: (a) Equipment diagram of fracture conductivity monitoring system; (b) API standard condutivity chamber and (c) Experimental flow chart.

6) Set the pumping flow rate of the fracturing fluid and sequentially establish the closure pressure applied to the artificial fractures, maintaining each pressure point for 30 minutes.
7) Initiate the ISCO pump to circulate the fracturing fluid, while the data acquisition system records pressure data feedback from the pressure difference sensor and the hydraulic press every second.

2.3 Experimental scheme

In this study, we conducted a series of experiments to investigate the fracture propagation mechanism of conglomerate samples under varying injection displacement and confining pressure conditions. A total of 9 experimental groups were established, encompassing sandy conglomerate, tuffaceous conglomerate, and dolomite conglomerate samples. Each lithology had three experimental groups, with the first group serving as the control. The control group maintained a maximum horizontal principal stress of 12 MPa, a minimum horizontal principal stress of 1 MPa, a vertical stress of 14 MPa, and a injection

Table 1. Physical model experiment scheme of true triaxial hydraulic fracturing.

Numbering	Types of rock samples	σ_h (MPa)	σ_H (MPa)	σ_V (MPa)	Injection rate (mL/min)
B-1	Dolomitic conglomerate	1	12	14	10
B-2		3	14	16	10
B-3		1	12	14	20
N-1	Tuffaceous conglomerate	1	12	14	10
N-2		3	14	16	10
N-3		1	12	14	20
S-1	Sandy conglomerate	1	12	14	10
S-1		3	14	16	10
S-3		1	12	14	20

flow rate of 10 mL/min. The second experimental group aimed to explore the effect of changes in in-situ stress on injection pressure and artificial fracture propagation morphology. Here, the maximum horizontal principal stress was increased to 14 MPa, the minimum horizontal principal stress to 3 MPa, the vertical stress to 16 MPa, with the injection flow rate remaining at 10 mL/min. Finally, the third group investigated the impact of varying injection rates on injection pressure and fracture morphology, with the injection flow rate increased to 20 mL/min while maintaining the same in-situ stress as the first group. The specific experimental configurations are summarized in Table 1.

The fracture conductivity experiment aims to investigate the impact of reservoir lithology, sand concentration, and confining pressure on fracture conductivity. Using 30/50 mesh proppant, three experimental groups were established for each lithology of conglomerate. The sand concentrations were set at 2, 4, and 6 kg/m^2, respectively. Fracture conductivity variations were examined as confining pressure increased from 10 to 50 MPa. The experimental setup is outlined in Table 2.

3. Experimental results of true triaxial hydraulic fracturing physical model

3.1 Injection pressure response

As shown in Fig. 5, it is the injection pressure curve of three sets of hydraulic fracturing experiments of dolomitic conglomerate. Among them, the maximum horizontal principal stress, the minimum horizontal principal stress and the vertical stress applied by the B1 rock sample are 12, 1, and 14 MPa, respectively, and the injection rate is 10 mL/min. From Fig. 5, it can be seen that in the early stage of liquid injection, the pressure in the wellbore increased slowly, and then the pressure in the wellbore increased rapidly. When the pressure in the wellbore reached 9.83 MPa, the rock sample ruptured, and then the pressure decreased rapidly and remained around 0.1 MPa.

In contrast to the experimental conditions of sample B1, for sample B2, the hydraulic fracturing experiment involves increasing the geostress while keeping the injection flow rate constant. Compared to the injection pressure curve of sample B1, the breakdown response curves of both samples generally exhibit similar trends. However, for sample B2, the breakdown pressure reached 11.86 MPa. Additionally, after the wellbore pressure dropped to 2.23 MPa, it gradually decreased further until stabilizing around 0.1 MPa.

The rise in ground stress elevates the effective stress within the rock sample, thereby enhancing its compressive strength and subsequently raising the breakdown pressure (Yu et al., 2024). Following the breakdown of the rock sample, the rapid drop in well pressure occurs, and the fractures close due to the impact of elevated ground stress, impeding the swift discharge of fracturing fluid.

Compared to the experimental conditions of the B1 rock sample, the B3 sample increases the injection rate while maintaining the in-situ stress unchanged. Observing the figure, we note that during the initial liquid injection phase, the borehole pressure increment closely mirrors that of the B1 sample. However, around 30 seconds into injection, the pressure within the B3 rock sample surges rapidly, culminating in a final breakdown pressure of 9.86 MPa. Notably, the rupture time for the B3 sample is approximately 50 seconds, while that of the B1 sample is around 80 seconds, indicating that the B3 sample ruptures in half the time compared to the B1 sample.

In contrast to the experimental conditions of sample B1, sample B3 maintained a constant confining stress while increasing the injection volume. From Fig. 5, it is evident that initially, the rate of pressure increase inside the wellbore for sample B3 was similar to that of sample B1. However, around 30 seconds into injection, the pressure inside the wellbore for sample B3 rapidly rose. Ultimately, the rock sample fractured at a pressure of 9.86 MPa. Sample B3 fractured in approximately 50 seconds, whereas sample B1 took about 80 seconds to fracture. Therefore, under these conditions, sample B3 fractured in half the time compared to sample B1.

Fig. 6 shows the injection pressure response curves from three tuffaceous conglomerate experiments. The breakdown pressure for the N1 rock sample is 8.81 MPa. When the injection rate remains constant but the in-situ stress is increased, the N2 sample's breakdown pressure rises to 11.59 MPa.

Table 2. Physical model experiment scheme of true triaxial hydraulic fracturing.

Types of rock samples	Sand concentration (kg/m^2)	Confining pressure (MPa)				
Dolomitic conglomerate	2	10	20	30	40	50
	4	10	20	30	40	50
	6	10	20	30	40	50
Tuffaceous conglomerate	2	10	20	30	40	50
	4	10	20	30	40	50
	6	10	20	30	40	50
Sandy conglomerate	2	10	20	30	40	50
	4	10	20	30	40	50
	6	10	20	30	40	50

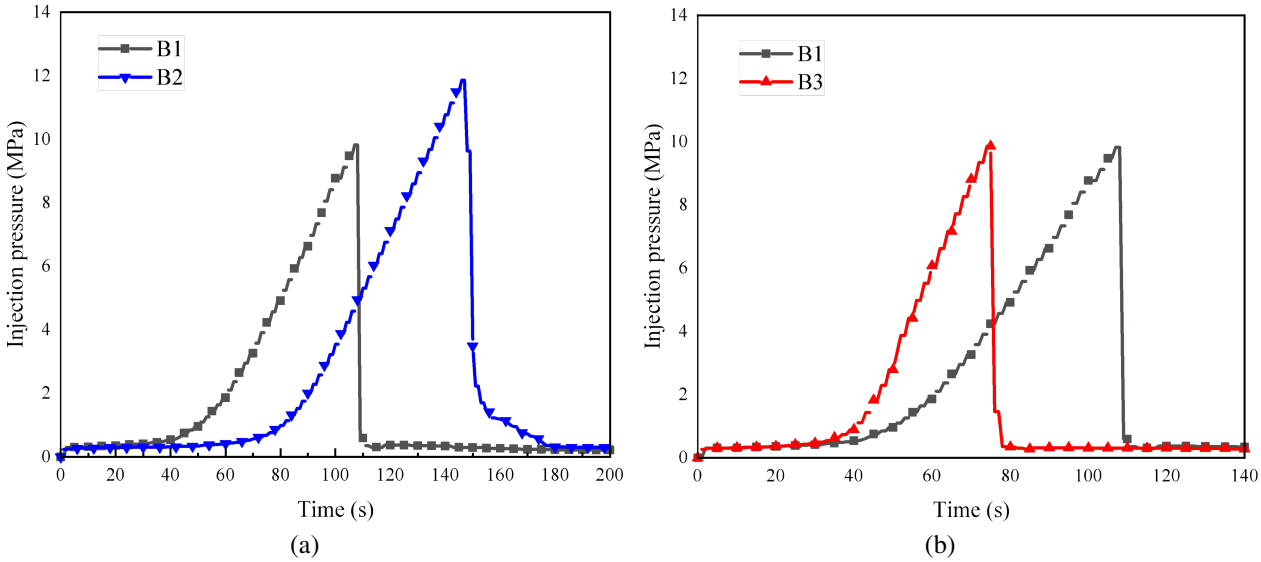

Fig. 5. Hydraulic fracturing experimental results of dolomitic conglomerate samples: (a) the injection rate is the same, but the ground stress is different and (b) the same ground stress, different injection rate.

Unlike the dolomitic conglomerate, the injection pressure of the N2 rock sample does not exhibit a gradual decline after breakdown, and its crack initiation rate is slightly slower than that of the N1 sample. Furthermore, when the in-situ stress is kept constant but the injection rate is increased, the N3 rock sample's breakdown pressure significantly rises to 9.87 MPa, accompanied by a notable increase in the crack initiation rate.

In Fig. 7, the pressure response curves of three sandy conglomerate experiments are presented. The breakdown pressure of rock sample S1 registers 8.69 MPa, with approximately 50 s elapsing from the onset of pressure to the collective fracture time of the rock. Conversely, with an increase in in-situ stress, the breakdown pressure of the S2 rock sample diminishes to 8.02 MPa, although the crack initiation speed of the rock samples remains largely consistent with that of S1. Moreover, the wellbore pressure after fracture of the S2 rock sample also exhibits a gradual decline phase. Upon augmenting the injection rate, the breakdown pressure of the S3 rock sample measures 8.77 MPa, with roughly 30 s from the initiation of pressure to the collective fracture time of the rock.

From the pressure response curves of the nine true triaxial hydraulic fracturing experiments, it's evident that increasing the injection rate accelerates the time to rock fracture. For instance, in dolomitic conglomerate, breakdown pressure time reduced from 80 to 50 s, in tuffaceous conglomerate from 50 to 30 s, and in sandy conglomerate from 50 to 30 s. Doubling the injection rate halves the time for rock to fracture. Moreover, elevating in-situ stress not only boosts rock breakdown pressure but also slows down the decline rate of wellbore pressure post-fracture. Notably, samples B2 and S2 exhibit gradual well pressure decline post-fracture, attributed to the sudden pressure drop upon rock sample fracture, causing closure under higher ground stress, impeding rapid fracturing fluid discharge.

Fig. 8 shows the breakdown pressures of conglomerate rocks under different conditions and rock types. It's evident that increasing ground stress or injection rate enhances the

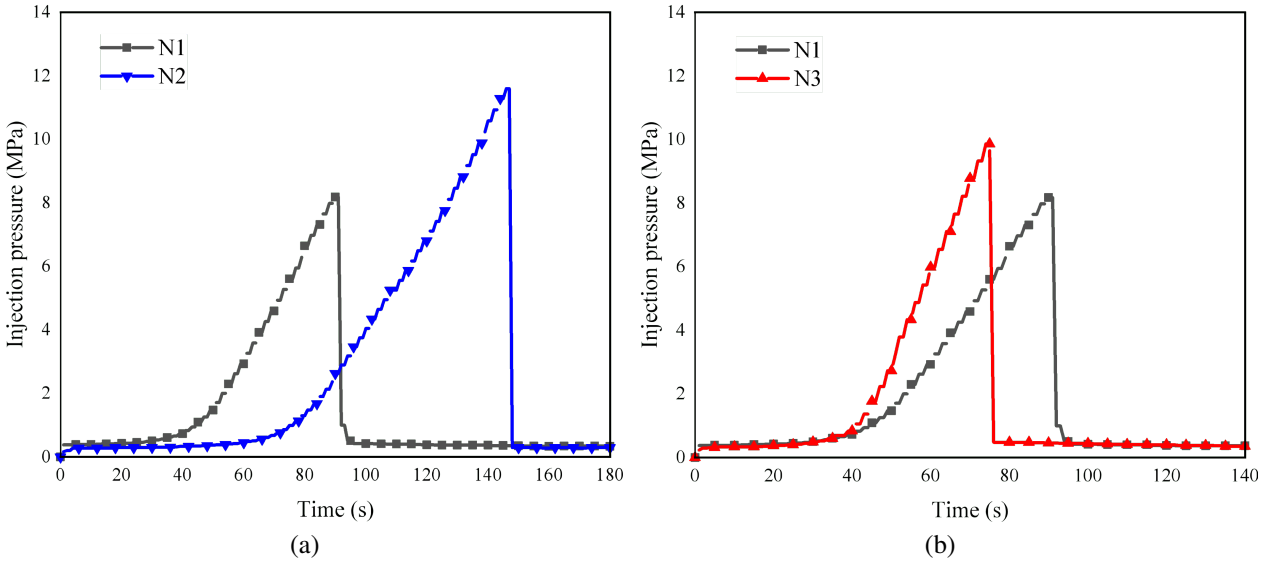

Fig. 6. Hydraulic fracturing experimental results of tuffaceous conglomerate samples: (a) the injection rate is the same, but the ground stress is different and (b) the same ground stress, different injection rate.

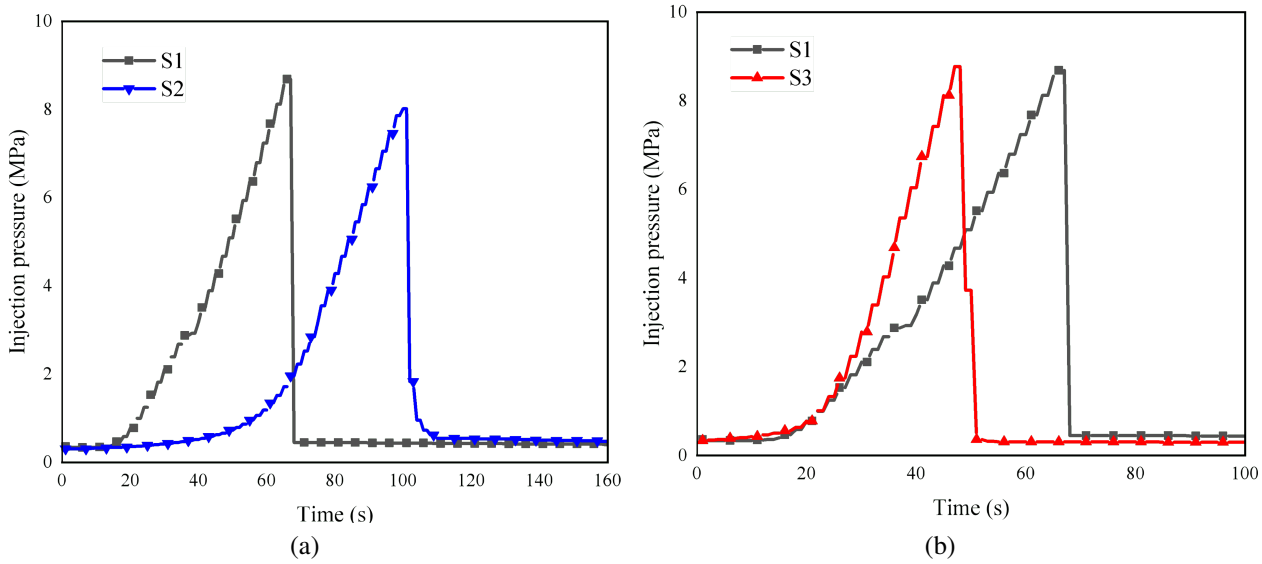

Fig. 7. The experimental results of hydraulic fracturing of conglomerate rock samples: (a) the injection rate is the same, but the ground stress is different and (b) the same ground stress, different injection rate.

breakdown pressure, yet the rise in ground stress is more advantageous. Overall, the breakdown pressure hierarchy among different lithology conglomerates is as follows: Dolomitic Conglomerate > Tuffaceous Conglomerate > Sandy conglomerate.

3.2 Fracture propagation morphology

The dolomite conglomerate B1 rock sample is depicted in Fig. 9(a). The initiation of artifical fracture occurs from the open hole section and extends along the direction of the applied maximum horizontal principal stress, forming an inclined crack at a certain angle to the wellbore. Upon increasing the in-situ stress applied to the rock sample, as depicted in Fig. 9(b) for the B2 rock sample, the inclination angle between the fracture and the wellbore increases. However, the fracture still propagates along the direction of the maximum horizontal principal stress. When keeping the in-situ stress unchanged and increasing the injection rate, as shown in Fig. 9(c) for the B3 rock sample, the fractures initiate from the open hole section and propagate along the direction of the maximum horizontal principal stress. Additionally, the fractures in the B3 rock sample appear longer compared to those in the B1 rock sample.

The fracture morphology of tuffaceous conglomerate is depicted in Fig. 10. The N1 group experiment is illustrated in Fig. 10(a). Compared to dolomite conglomerate, the fractures

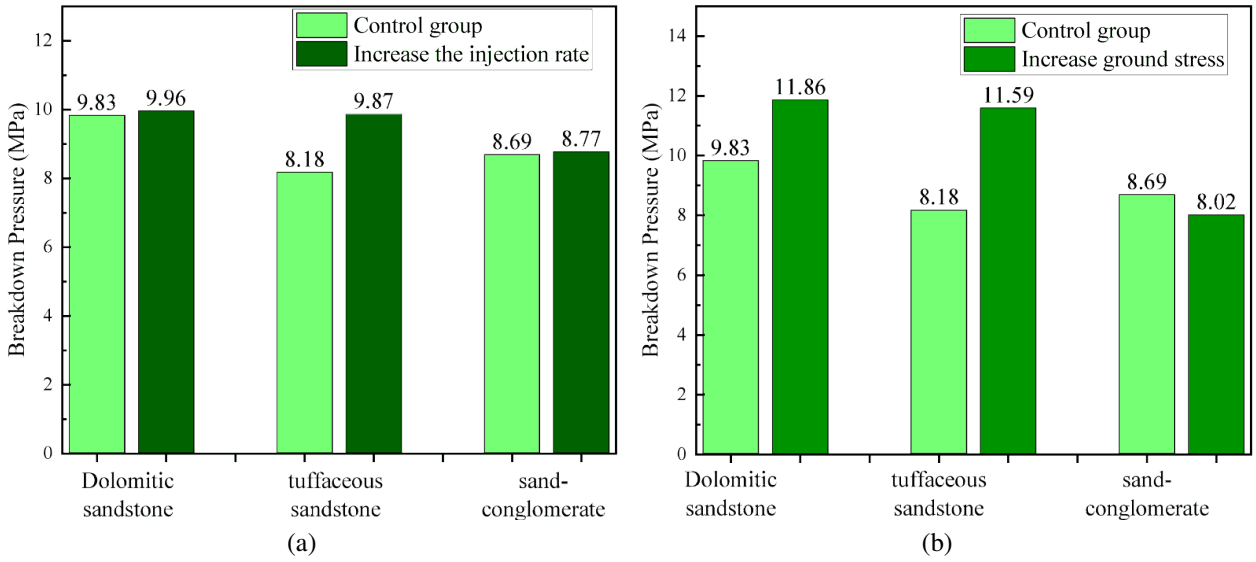

Fig. 8. Comparison of fracture pressure of different lithology conglomerate: (a) increase the ground stress and (b) increasing the injection rate.

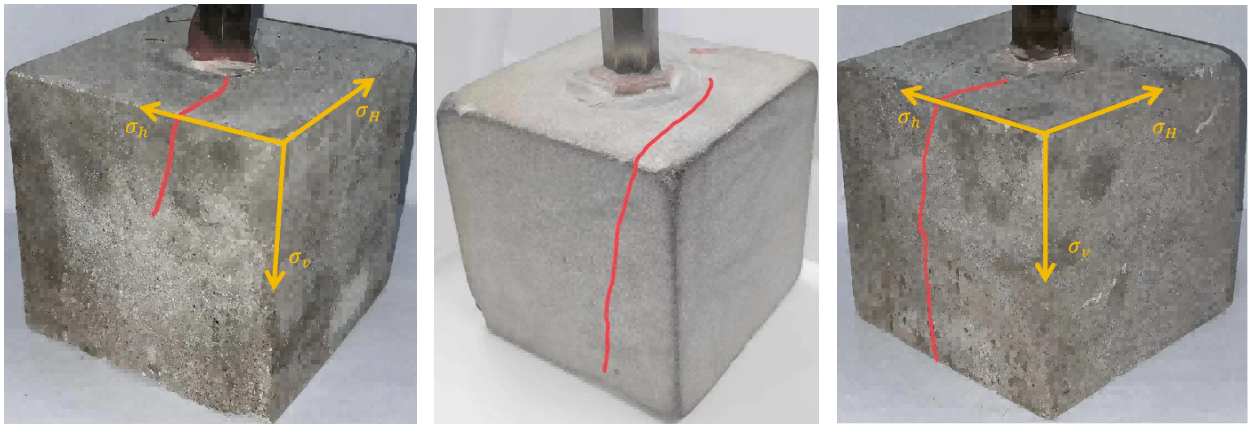

Fig. 9. Fracture morphology of dolomitic conglomerate: (a) B1 rock sample; (b) B2 rock sample and (c) B3 rock sample.

formed in tuffaceous conglomerate are wider, and the dip angle between the tuffaceous conglomerate and the wellbore is smaller. When the in-situ stress is increased, as shown in Fig. 10(b), the fracture dip angle of tuffaceous conglomerate is smaller than that of dolomitic conglomerate under the same experimental conditions, yet the fracture is more pronounced. Particularly, in the case of increasing the injection rate, as observed in the experimental results of the N3 rock sample shown in Fig. 10(c), the rock sample not only produces a fracture parallel to the direction of the maximum horizontal principal stress but also generates a macroscopic fracture inclined to the wellbore.

The fracture morphology of each rock sample is illustrated in Fig. 12. From a visual standpoint, the fractures induced by the conglomerate rock sample predominantly propagate along the gravel edges of the conglomerate surface. These fractures exhibit greater complexity and narrower widths compared to the other two rock samples. However, the mode of fracture propagation aligns with the direction of the maximum horizontal principal stress. In the S2 group experiment depicted in Fig. 12(b), the presence of natural fractures is evident, with artifical fractures initiating from the open-hole casing and propagating parallel to the horizontal plane. The sample diagram of the S2 group before the experiment is displayed in Fig. 11, revealing noticeable natural fractures in the horizontal direction on the surface of the rock sample.

To better visualize the propagation morphology of artifical fractures, the rock sample underwent computed tomography (CT) scanning after the experiment, and the fractures within the rock sample were reconstructed and modeled using AVIZO software, as depicted in Fig. 13. In comparison with the results of fracture morphology observed by the naked eye in Figs. 9-12, CT scanning also enabled the identification of some fine artificial fractures that were not visually discernible (as

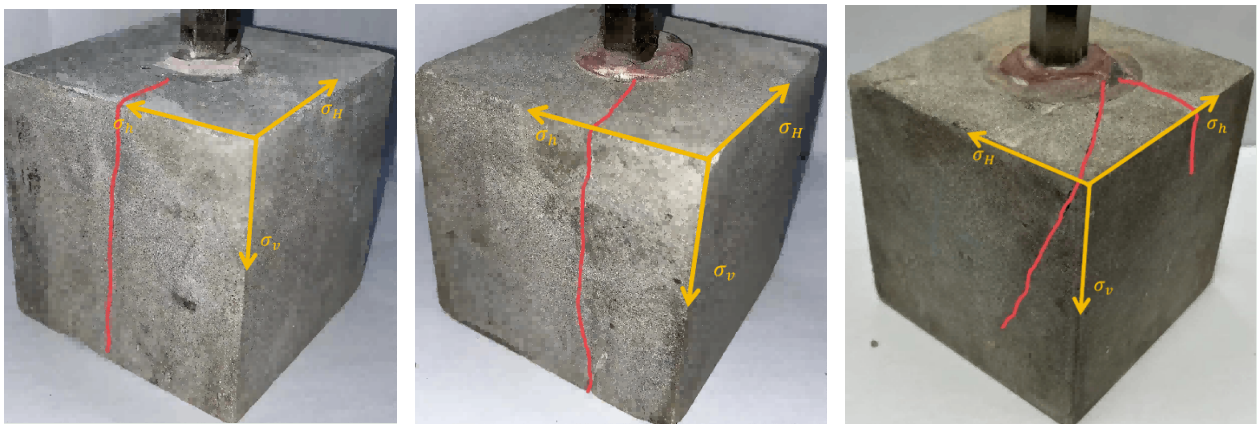

(a) (b) (c)

Fig. 10. Fracture morphology and CT scan of tuffaceous conglomerate: (a) N1 rock sample; (b) N2 rock sample and (c) N3 rock sample.

indicated in the circled area in Fig. 13).

Fig. 11. S2 rock sample before the experiment.

The analysis reveals that most fractures induced in dolomitic conglomerate and tuffaceous conglomerate are single fractures. In contrast, in sandy conglomerate, the presence of large gravel particles renders the interior relatively loose, with a more porous structure. Artifical fractures initiate from the open hole section and continuously traverse the natural weak surfaces between the conglomerate's large particles. Consequently, the majority of fractures exhibit irregular migration, ultimately forming a complex micro-fracture network. However, most artifical fractures in conglomerate are relatively small, with CT scan results indicating a plethora of disordered fracture structures, particularly evident in the experimental outcomes of S2 rock samples, as depicted in Fig. 13(h).

By observing the CT images of nine sets of true triaxial hydraulic fracturing experiments, it is evident that regardless of the lithology of the conglomerate gravel, hydraulic fractures propagate along the direction of maximum horizontal principal stress in the absence of natural fracture interference. Maintaining a constant injection rate, increasing the confining pressure prompts hydraulic fractures to propagate over longer distances. Conversely, keeping the confining pressure constant while increasing the injection rate results in more complex fracture morphologies. Furthermore, observations from CT images indicate that in breccia with small gravel diameters, such as dolomitic sandstone and tuffaceous sandstone, the fracture propagation mostly forms a single macroscopic fracture. However, in sandy conglomerates, the fracture morphology is not distinct. This phenomenon is generally consistent with the findings of Li et al. (2013) and Gong et al. (2019).

4. Experimental results of conductivity

4.1 Proppant embedment

As depicted in Fig. 14, it illustrates the distribution and embedding of proppant within dolomitic conglomerate at various sand concentration levels. The figure reveals that the rock structure of dolomitic conglomerate is relatively uniform, with the embedded proppant distributed across the entire surface of the rock plate in a relatively uniform manner. Furthermore, at lower sand concentration levels (2 kg/m^2), there is a smaller number of embedded proppant particles observed on the guide plate. However, as the sand concentration increases, the quantity of embedded proppant gradually rises. Notably, at a sand concentration of 6 kg/m^2, the highest amount of embedded proppant is observed.

As depicted in Fig. 15, the proppant embedding within tuffaceous conglomerate exhibits similarities to that of dolomitic conglomerate. The lithological characteristics of tuffaceous conglomerate result in a distribution of proppant particles that is spread across the surface of the rock sample, presenting a relatively uniform pattern overall. Moreover, similar to dolomitic conglomerate, the quantity of embedded proppant increases with rising sand concentration levels. However, it's worth noting that the overall amount of proppant embedding in tuffaceous conglomerate is less compared to

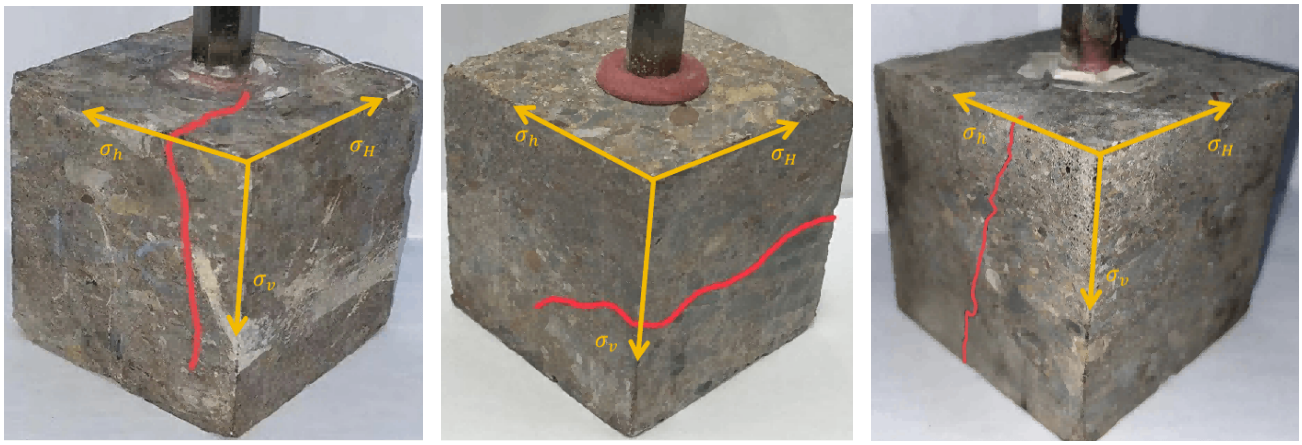

(a) (b) (c)

Fig. 12. Fracture morphology and CT scan of conglomerate: (a) S1 rock sample; (b) S2 rock sample and (c) S3 rock sample.

dolomitic conglomerate.

As illustrated in Fig. 16, the distribution and embedding of proppant within sandy conglomerate exhibit notable distinctions compared to dolomitic conglomerate and tuffaceous conglomerate. This discrepancy arises from the inherent non-uniformity of conglomerate rock structure, rendering the embedding of proppant into gravel challenging. Consequently, the distribution of embedded proppant in conglomerate appears to be more localized and concentrated in specific regions, likely due to the occurrence of internal fractures within the conglomerate rock mass.

4.2 Fracture conductivity change

Proppant embedment depth and distribution directly influence the effective width of the fracture, which subsequently affects fluid flow within the fracture. Fracture conductivity is commonly used to describe the fluid's ability to pass through the fracture. The equation for calculating the permeability of the proppant-filled layer under Darcy flow conditions is:

$$k = \frac{\mu QL}{99.998A\Delta p} \tag{1}$$

where k is the permeability of the proppant filling layer (μm^2); μ is the viscosity of the fluid at the test temperature (mPa·s); Q is the injection rate (cm^3/s); L is the length of fluid flow (cm); A is the cross-sectional area of the API fracture conductivity chamber (cm^2); and Δp is the pressure difference between the upstream and downstream pressures (kPa).

When the proppant filling layer is laid in the linear diversion chamber, the cross-sectional area is calculated by the equation:

$$A = \omega \cdot W_f \tag{2}$$

where, ω is the width of the fracture conductivity chamber (cm); W_f is the propped fracture width (cm).

The permeability of the proppant filling layer can be calculated by incorporating area A into Eq. (1).

$$k = \frac{\mu QL}{99.998\omega\Delta pW_f} \tag{3}$$

The conductivity of the proppant filling layer is the product of the fracture width and the permeability of the proppant filling layer. The width ω of the API fracture conductivity chamber is 3.81 cm, and the pressure port spacing L is 12.70 cm.

$$kW_f = \frac{5.55\mu QL}{\Delta p} \tag{4}$$

where kW_f is the conductivity of proppant filling layer (μm^2·cm).

Fig. 17 illustrates the variation in fracture conductivity of dolomitic conglomerate over time under different proppant concentrations. It's evident that at low confining pressures, fracture conductivity rises with increasing sand concentration. For instance, under a confining pressure of 10 MPa, when the sand concentration is 2 kg/m^2, conductivity measures 37 μm^2·cm, whereas at 6 kg/m^2, conductivity increases to 58 μm^2·cm, marking a roughly 1.6-fold increase. Across all sand concentrations, however, fracture conductivity declines as confining pressure rises, and the disparity in conductivity between different concentrations diminishes with increasing confining pressure. This phenomenon can be attributed to initial experimental stages where low confining pressures and short durations lead to conductivity gains with higher sand concentrations. Yet, as confining pressure mounts, proppants become gradually embedded or fractured within the rock plate, resulting in rearranged proppant arrangements, diminished inter-proppant gaps, and subsequent conductivity reduction. Consequently, the conductivity gap between varying sanding concentrations also diminishes over time.

Fig. 18 depicts the curve of fracture conductivity of tuffaceous conglomerate concerning confining pressure and time across various sand concentrations. Similar to dolomitic conglomerate, tuffaceous conglomerate exhibits an increase in conductivity with rising sand concentration at the onset of the experiment. For instance, under a confining pressure of 10 MPa, conductivity measures 32 μm^2·cm at a sand

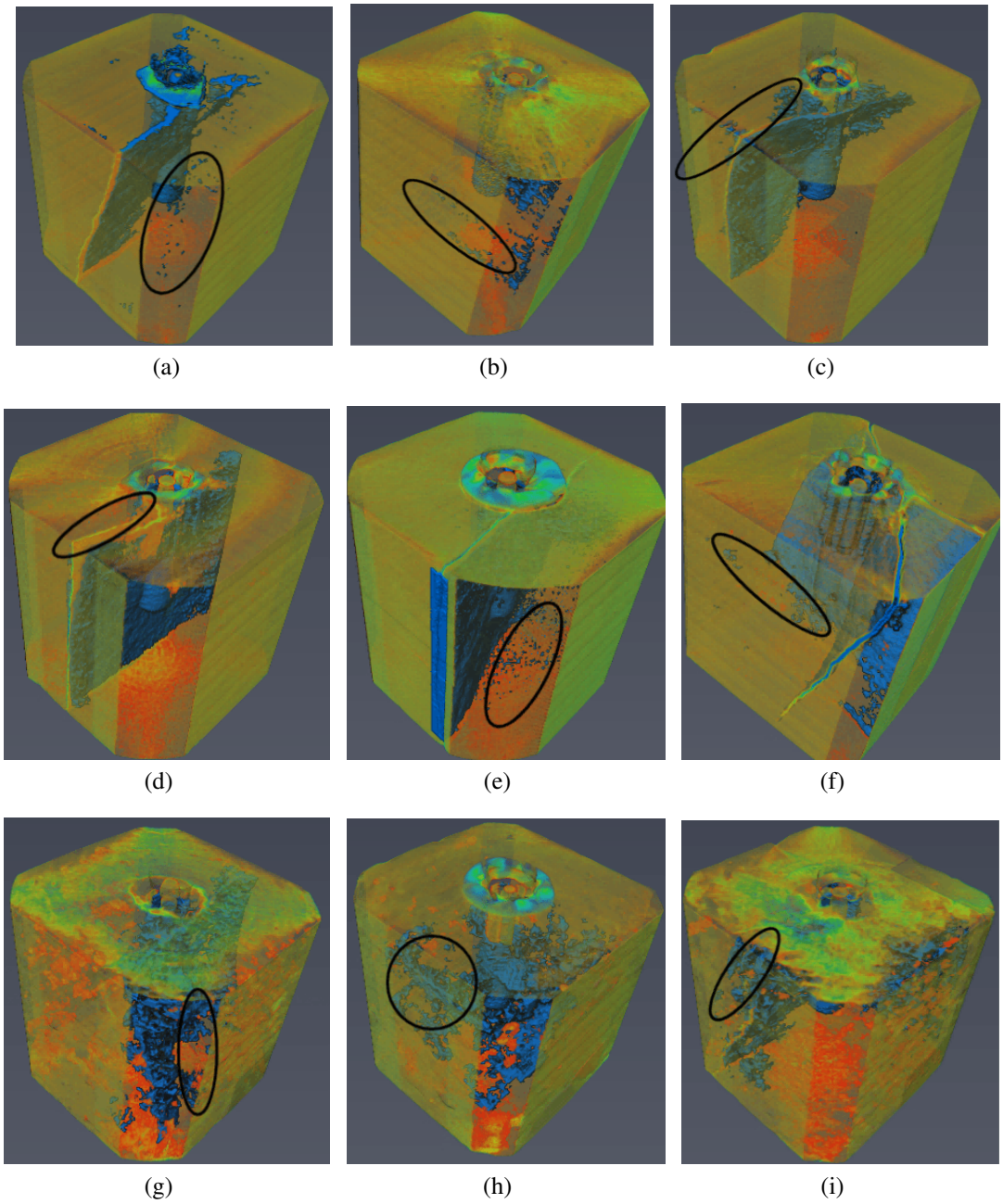

Fig. 13. Fracture propagation of conglomerate with different lithology under different conditions: (a) B1; (b) B2; (c) B3; (d) N1; (e) N2; (f) N3; (g) S1; (h) S2 and (i) S3.

concentration of 2 kg/m^2, while at 6 kg/m^2, conductivity elevates to 47 μm^2·cm, marking an approximate 1.5-fold increase. However, as confining pressure intensifies, fracture conductivity across different sand concentrations diminishes, leading to a reduction in the disparity of conductivity between varying sand concentrations.

In Fig. 19, the conductivity variation of sand conglomerate with respect to confining pressure and time across different sand concentrations is depicted. As the confining pressure escalates from 10 to 50 MPa, there is a gradual decline in fracture conductivity. Notably, when the confining pressure stands at 10 MPa, the fracture conductivity registers its peak value. This phenomenon is attributed to the low confining pressure resulting in larger fracture width and inter-proppant gaps, thereby minimizing fluid flow resistance and maximizing fracture conductivity. Moreover, under equivalent confining pressures, the conductivity of artificial fractures also experiences enhancement with escalating sand concentration.

In summary, among the tested lithologies under equivalent sand concentrations, sandy conglomerate exhibits the highest conductivity, while the difference in conductivity between dolomitic conglomerate and tuffaceous conglomerate is marginal. This can be attributed to the robust hardness of gravel particles within sandy conglomerate. Under confining

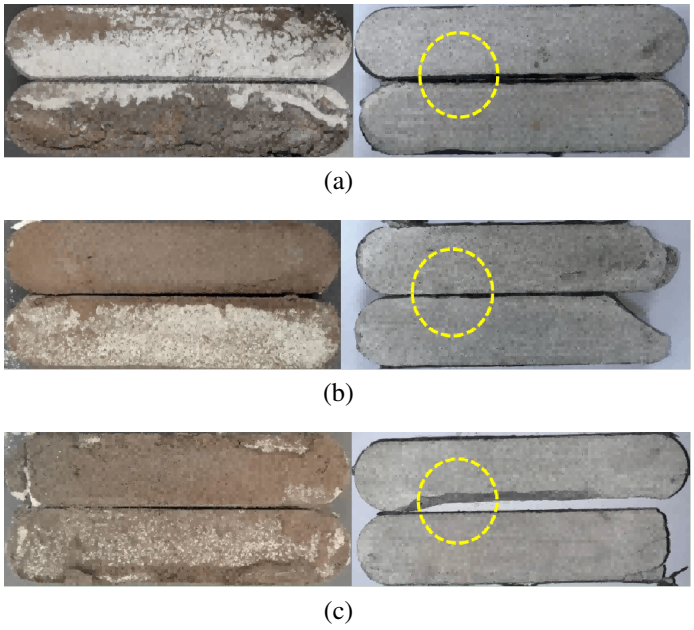

Fig. 14. Proppant embedment in dolomitic conglomerate under different sanding concentrations: (a) sand concentration 2 kg/m^2; (b) sand concentration 4 kg/m^2 and (c) sand concentration 6 kg/m^2.

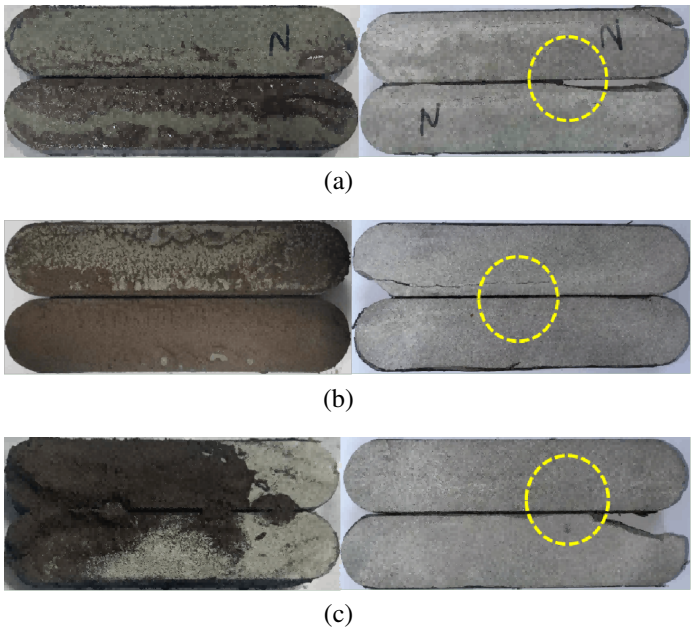

Fig. 15. Proppant embedment in dolomitic conglomerate under different sanding concentrations: (a) sand concentration 2 kg/m^2; (b) sand concentration 4 kg/m^2 and (c) sand concentration 6 kg/m^2.

pressure, the reduction in embedded proppant quantity within the rock plate results in heightened conductivity in sandy conglomerate. Furthermore, there's a decreasing trend in rock plate conductivity with increasing confining pressure, whereas an opposite trend is observed with rising sand concentration. Specifically, as sand concentration escalates from 2 to 6 kg/m^2, the artificial fracture conductivity elevates to approximately 1.5 times its original value.

5. Conclusions

In this study, we utilized the physical model experiment system for true triaxial hydraulic fracturing and the fracture conductivity test device to conduct experiments on hydraulic fracturing and conductivity loss in three distinct types of conglomerates. We aimed to investigate the variation in fracture propagation morphology and conductivity characteristics across different lithologies of conglomerate. The key findings of our study are summarized as follows:

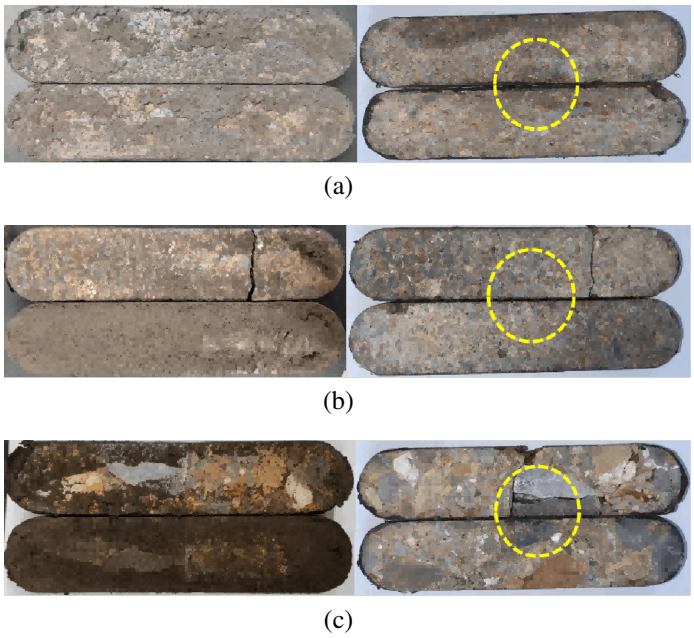

Fig. 16. Proppant embedment under different sand concentration of conglomerate: (a) sand concentration 2 kg/m^2; (b) sand concentration 4 kg/m^2 and (c) sand concentration 6 kg/m^2.

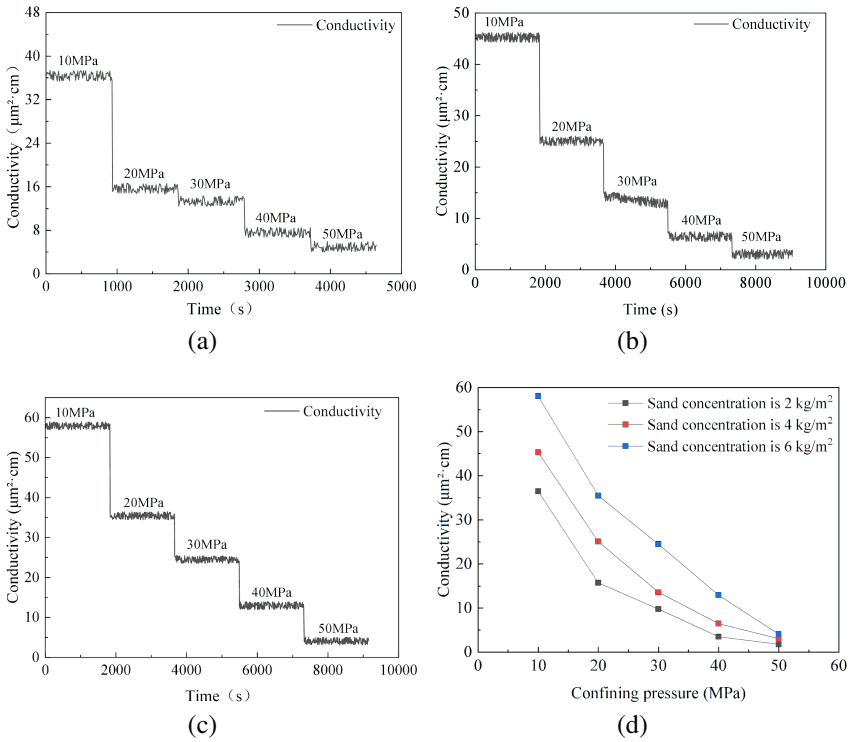

Fig. 17. Variation of conductivity of dolomitic conglomerate with time and confing pressure: (a) 2 kg/m^2 sand concentration ; (b) sand concentration 4 kg/m^2; (c) sand concentration 6 kg/m^2 and (d) the variation curve of conductivity with confining pressure under different sand concentration.

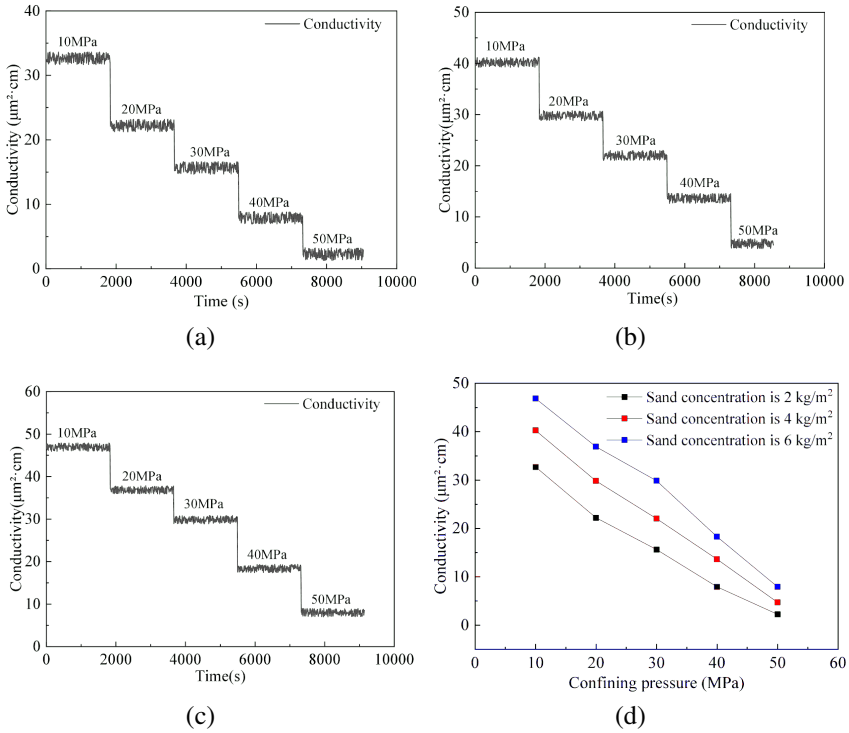

Fig. 18. Variation of conductivity of tuffaceous conglomerate with time: (a) sand concentration 2 kg/m^2; (b) sand concentration 4 kg/m^2; (c) sand concentration 6 kg/m^2 and (d) the variation curve of conductivity with confining pressure under different sand concentration.

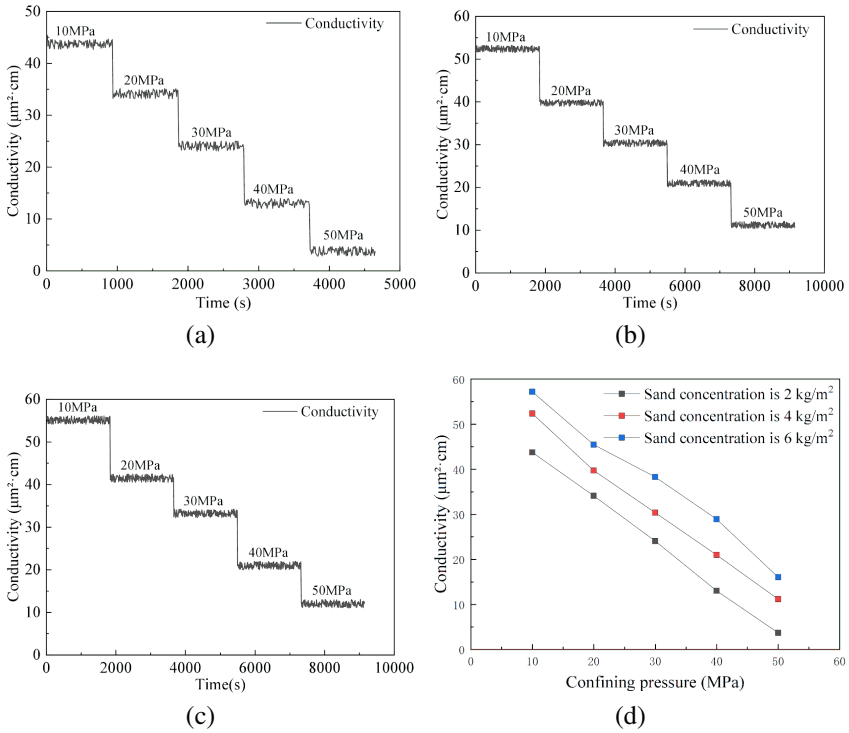

Fig. 19. Variation of the conductivity of conglomerate with time: (a) sand concentration 2 kg/m^2; (b) sand concentration 4 kg/m^2; (c) sand concentration 6 kg/m^2 and (d) the variation curve of conductivity with confining pressure under different sand concentration.

1) In the absence of natural fractures, dolomitic conglomerate, tuffaceous conglomerate, and sandy conglomerate all exhibit fracture initiation from the open hole section, propagating along the direction of maximum horizontal principal stress. However, there is a notable difference in fracture morphology among these lithologies. Dolomitic conglomerate and tuffaceous conglomerate tend to form singular macroscopic fractures. In contrast, the fractures in sandy conglomerate navigate around gravel particles during expansion due to the abundance of these particles within the rock mass. This results in the formation of a relatively intricate network of smaller fractures.
2) The experimental findings indicate that increasing the in-situ stress or injection rate results in a certain increase in fracture pressure for conglomerate samples. However, enhancing the in-situ stress is more effective in boosting breakdown pressure. Overall, the breakdown pressure ranking among different lithology conglomerates is as follows: dolomitic conglomerate > tuffaceous conglomerate > sandy conglomerate. Additionally, while increasing the injection rate may not significantly enhance rock breakdown pressure, it effectively reduces the time required to reach the breakdown pressure. Doubling the injection rate results in approximately halving the breakdown time of the rock sample;
3) The fracture conductivity decreases with increasing confining pressure across all lithologies, and this loss of fracture conductivity is irreversible. Initially, when the confining pressure is low, the gap between proppants is large, resulting in minimal fluid flow resistance and high fracture conductivity. However, the substantial gap between proppants also renders the fracture more susceptible to closure under confining pressure, leading to a significant decrease in fracture conductivity at the onset of the experiment.
4) The fracture conductivity of sandy conglomerate surpasses that of dolomitic conglomerate and tuffaceous conglomerate significantly. This is attributed to the presence of high-hardness gravel particles of various sizes scattered irregularly throughout the conglomerate. Embedding proppant particles into the surface of these gravel particles proves challenging, resulting in heightened fracture conductivity within conglomerate formations. Furthermore, irrespective of lithology, fracture conductivity escalates with increasing sand concentration. Experimental findings indicate that augmenting sand concentration from 2 to 6 kg/m^2 boosts the fracture conductivity of the supporting fracture to approximately 1.5 times its original value.

Author information

The email addresses of the remaining authors of this paper are as follows:

lxiaoshan@petrochina.com.cn (X. Li);
zhangjinxj@petrochina.com.cn (J. Zhang);
fcbazc@petrochina.com (Z. Ba).

Acknowledgements

This work was supported financially by the National Natural Science Foundation of China (No. 52274002), the Beijing Natural Science Foundation Project (No. 3222030), the PetroChina Science and Technology Innovation Foundation Project (2021DQ02–0201), and the Research and Technology Development Project of China Petroleum & Natural Gas Corporation (No. 2021DJ1003).

Conflict of interest

The authors declare no competing interest.

References

Cai, J., Zhao, L., Zhang, F., et al. Advances in multiscale rock physics for unconventional reservoirs. Advances in Geo-Energy Research, 2022, 6(4): 271-275.

Chen, B., Barboza, B. R., Sun, Y., et al. A review of hydraulic fracturing simulation. Archives of Computational Methods in Engineering, 2022, 29(4): 1-58.

Chen, S. Study on sand production characteristics of conglomerate reservoir. Beijing, China University of Petroleum, 2022.

Cooke Jr, C. E. Conductivity of fracture proppants in multiple layers. Journal of Petroleum Technology, 1973, 25(9): 1101-1107.

Fan, M., Mcclure, J., Institute, V. P., et al. Using an experiment/simulation-integrated approach to investigate fracture-conductivity evolution and non-darcy flow in a proppant-supported hydraulic fracture. SPE Journal, 2019, 24(04): 1912-1928.

Geertsma, J., De Klerk, F. A rapid method of predicting width and extent of hydraulically induced fractures. Journal of Petroleum Technology, 1969, 21(12): 1571-1581.

Gong, T., Xia, B., Liu, L., et al. Propagation of hydraulic fracture under the joint impact of bedding planes and natural fractures in shale reservoirs. Energy Science & Engineering, 2019, 7(6): 2690-2702.

He, M. The future of rock mechanics lies with China: Inaugural editorial for Rock Mechanics Bulletin. Rock Mechanics Bulletin, 2022, 1: 100010.

Jiang, Y., Li, B., Wang, C., et al. Advances in development of shear-flow testing apparatuses and methods for rock fractures: A review. Rock Mechanics Bulletin, 2022, 1(1): 100005.

Li, J., Tang, Y., Wu, T., et al. Overpressure origin and its effects on petroleum accumulation in the conglomerate oil province in Mahu Sag, Junggar Basin, NW China. Petroleum Exploration and Development, 2020, 47(4): 726-739.

Li, L., Meng, Q., Wang, S., et al. A numerical investigation of the hydraulic fracturing behaviour of conglomerate in Conglomerate formation. Acta Geotechnica, 2013, 8(6): 597-618.

Li, Q., Zhang, C., Yang, Y, et al. Preliminary experimental investigation on long-term fracture conductivity for evaluating the feasibility and efficiency of fracturing operation in offshore hydrate-bearing sediments. Ocean Engineering, 2023, 281: 114949.

Li, Z., Zhao Q., Teng, Y., et al. Experimental investigation of non-monotonic fracture conductivity evolution in energy georeservoirs. Journal of Petroleum Science and Engineering, 2022, 211: 110103.

Lian, Z., Zhang, J., Wang, X., et al. Simulation study of characteristics of hydraulic fracturing propagation. Rock and Soil Mechanics, 2009, 30(1): 169-174.

Liu, G. Challenges and countermeasures of log evaluation in unconventional petroleum exploration and development. Petroleum Exploration and Development, 2021, 48(5): 1033-1047.

Liu, K., He, H., Yin, D. Theoretical and experimental study on the long-term conductivity of heterogeneous artificial fractures in tight reservoirs. Energy Reports, 2023, 9: 3881-3895.

Liu, Y., Tang, D., Xu, H., et al. The impact of coal macrolithotype on hydraulic fracture initiation and propagation in coal seams. Journal of Natural Gas Science and Engineering, 2018, 56: 299-314.

McDaniel, B. W. Conductivity testing of proppants at high temperature and stress. SPE Western Regional Meeting. Paper SPE 15067 Presented at the SPE California Regional Meeting, Oakland, California, 2–4 April, 1986.

Meng, Q., Zhang, S., Guo, X., et al. A primary investigation on propagation mechanism for hydraulic fractures in conglomerate formation. Journal of Oil and Gas Technology, 2010, 32(4): 119-123.

Stegent, N. A. , Wagner, A. L., Mullen, J., et al. Engineering a successful fracture-stimulation treatment in the eagle ford shale. Paper SPE 136183 Presented at the Tight Gas Completions Conference, San Antonio, Texas, USA, 2-3 November, 2010.

Shi, X., Qin, Y., Gao, Q., et al. Experimental study on hydraulic fracture propagation in heterogeneous conglomerate rock. Geoenergy Science and Engineering, 2023, 225: 211673.

Sun, H. Study on the conductivity of conglomerate artificial fracture. Beijing, China University of Petroleum, 2022.

Wang, Z., Lin, B., Chen, G., et al. Experimental study on evaluation of conglomerate reservoir support-type fracture conductivity in Xinjiang oilfield. Energy, 2023, 278: 127877.

Wang, D., Ge, H., Wang, X., et al. A novel experimental approach for fracability evaluation in tight-gas reservoirs. Journal of Natural Gas Science and Engineering, 2015, 23: 239-249.

Wang, Q., Wang, D., Fu, W., et al. Effects of saturated fluids on petrophysical properties of hot dry rock at high temperatures: An experimental study. Geothermics. 2024a, 121: 103048.

Wang, Q., Wang, D., Yu, B.,et al. Evolution of elastic–plastic characteristics of rocks within middle-deep geothermal reservoirs under high temperature. Natural Resources Research. 2024b, 6: 1-24.

Wang, D., Qu, Z., Liu, C., et al. A numerical investigation into the propagation of acid-etched wormholes in geothermal wells. Unconventional Resources, 2024: 100083.

Wang, D., Zhou, F., Dong, Y., et al. Experimental Investigation of Thermal Effect on Fracability Index of Geothermal Reservoirs. Natural Resources Research, 2021, 30(1): 273-288.

Wang, J., Huang, Y., Zhou, F., et al. The influence of proppant breakage, embedding, and particle migration on fracture conductivity. Journal of Petroleum Science and Engineering, 2020, 193: 107385.

Wang, X., Hu, Y., Li, S., et al. Models for Conductivity and Productivity of Hydraulic Fractures in Tight Oil Reservoirs in Sedimentary Rocks. Xinjiang Petroleum Geology, 2023, 44(4): 442-449.

Xie, H., Lu, Y., Yin, X., et al. Flow conductivity of acid etching fracture of the conglomerates with various gravel content. Reservoir Evaluation and Development, 2011, 1(5): 40-42.

Yang, C., Liu, J. Petroleum rock mechanics: An area worthy of focus in geo-energy research. Advances in Geo-Energy Research, 2021, 5(4): 351-352.

Yu, J., Li, N., Hui, B., et al. Experimental simulation of fracture propagation and extension in hydraulic fracturing: A state-of-the-art review. Fuel, 2024, 363: 131021.

Zhi, D., Tang, Y., He, W., et al. Orderly coexistence and accumulation models of conventional and unconventional hydrocarbons in Lower Permian Fengcheng Formation, Mahu sag, Junggar Basin. Petroleum Exploration and Development, 2021, 48(1): 43-59.

Zhou, Z., Wang, G. D., Zheng, B., et al. Comparative experimental investigation on permeability and pressure bearing capacity of different types of temporary plugging bodies. Unconventional Resources, 2024, 4: 100062.

Zou, Y., Shi, S., Zhang, S., et al. Experimental modeling of sanding fracturing and conductivity of propped fractures in conglomerate: A case study of tight conglomerate of Mahu sag in Junggar Basin, NW China. Petroleum Exploration and Development, 2021, 48(6): 1383-1392.